

## Article

# Influence of Growth Parameters on the Electrochemical Performance of Electrodeposited Carbons

Jimmy Wu <sup>1</sup>, Matthew A. Hughes <sup>2</sup>, Neeraj Sharma <sup>1,\*</sup>  and Jessica Allen <sup>2</sup> 

<sup>1</sup> School of Chemistry, University of New South Wales, Sydney, NSW 2052, Australia; jimmy.wu@unsw.edu.au

<sup>2</sup> School of Chemical Engineering, Newcastle Institute for Energy and Resources, University of Newcastle, Callaghan, NSW 2308, Australia; matthew.a.hughes@uon.edu.au (M.A.H.); j.allen@newcastle.edu.au (J.A.)

\* Correspondence: neeraj.sharma@unsw.edu.au

**Abstract:** Generating useful chemicals from CO<sub>2</sub> is driving research into carbon capture and utilization. In this work, hard carbons are electrodeposited on various substrates from molten carbonate melts in CO<sub>2</sub> atmospheres. These electrodeposited carbons are subsequently used as anodes in sodium-ion batteries, with preliminary investigations into their performance in potassium-ion batteries. The hard carbons were characterized using X-ray diffraction (XRD) and Raman spectroscopy. Hard carbons grown on graphite substrates produced initial reversible capacities of 405 ± 29 mAh/g and capacity retention of 85.2 ± 1.1% after 50 cycles when cycled at 10 mA/g which are amongst the highest capacities reported for hard carbons to date. This work clearly illustrates that the carbons generated via CO<sub>2</sub> mediated electrodeposition are suitable for application in next generation batteries.

**Keywords:** sodium-ion; anode; hard carbon; eutectic melt; ternary carbonate; electrochemical deposition



**Citation:** Wu, J.; Hughes, M.A.; Sharma, N.; Allen, J. Influence of Growth Parameters on the Electrochemical Performance of Electrodeposited Carbons. *Batteries* **2022**, *8*, 81. <https://doi.org/10.3390/batteries8080081>

Academic Editor: Torsten Brezesinski

Received: 7 June 2022

Accepted: 18 July 2022

Published: 29 July 2022

**Publisher's Note:** MDPI stays neutral with regard to jurisdictional claims in published maps and institutional affiliations.



**Copyright:** © 2022 by the authors. Licensee MDPI, Basel, Switzerland. This article is an open access article distributed under the terms and conditions of the Creative Commons Attribution (CC BY) license (<https://creativecommons.org/licenses/by/4.0/>).

## 1. Introduction

Rechargeable batteries based on lithium-ion technology dominate today's global markets due to their performance in portable electrochemical energy storage applications. Their continued success is due to their high energy density, low self-discharge rate, as well as their versatility to be scaled up from portable electronics to hybrid electric vehicles and grid storage systems [1–4]. However, continued arguments about the rising costs of raw materials means alternative portable energy solutions must be considered [5–7]. Sodium-ion batteries (NIBs) have been considered an alternative to LIBs in certain applications due to the higher natural abundance of Na and possible use of cheaper current collectors which drives down its overall costs [8].

Various carbon-based anodes are being evaluated as anodes for NIBs. Hard carbons are typically defined as disordered, amorphous, or non-organized and non-graphitic carbon-based compounds that do not graphitize after heating, even when heating to temperatures above 3000 °C [9], and they have been considered promising anodes for NIBs. Hard carbons are highly versatile, such that the synthesis of these can be achieved from a range of carbon-based materials [10], as well as biomass [11,12], which can reduce the overall environmental impact in the application.

Herein, hard carbons are synthesized via the reduction of a ternary eutectic which contain Li-, K- and Na-carbonates. The carbonate salts are heated to a molten state and carbons are then grown on a substrate with an electrochemical deposition process. This process is undertaken with a CO<sub>2</sub> flow [13]. CO<sub>2</sub> is a stable gas, formed from fossil fuels through exothermic combustion reactions. This is a theoretically reversible process, however, to revert CO<sub>2</sub> into stable compounds requires energy input, which can be achieved through electrolysis where CO<sub>2</sub> is converted through electrochemical reactions to carbon and oxygen.

Generally, the kinetics for the CO<sub>2</sub> to carbon and oxygen reaction are not favorable at low temperatures and favor partial reduction to carbon monoxide. For complete reduction

it is best to use both electrical inputs for the electrolysis, and to maintain the system at elevated temperatures [14]. Electrolysis in molten carbonates containing lithium carbonate results in generation of carbon at the cathode, being more thermodynamically favorable than metal deposition, while oxygen gas is evolved at the anode [13]. Through the use of carbonates and oxides as intermediate species, an efficient CO<sub>2</sub> capture and transformation process can be created. Furthermore, the carbonate salts have been demonstrated to capture and retain heat efficiently in concentrated solar thermal processes, so there is a possibility that the process can be driven by renewable energy inputs [15].

Previously, hard carbons generated by this method were shown to yield highly varied structural and electrochemical properties based on the deposition parameters used [16]. It is important to probe a variety of deposition parameter space in order to develop deposition-electrochemical performance relationships which can be used to design and tune ideal carbons for applications. Therefore, gold, copper, and graphitic substrates were used to synthesize hard carbons via electrodeposition, which were subsequently characterized electrochemically in sodium-ion batteries showing markedly improved performance. Investigations were also taken in potassium-ion batteries.

Overall, this work demonstrates the expansion of the experimental parameter space that can be used to produce viable carbons via electrodeposition. It illustrates how such parameters can be modified to alter subsequent electrochemical performance as electrodes in sodium-ion batteries. Thus, providing an avenue for further optimization.

## 2. Experimental

Hard carbons were deposited via an electrochemical method using a ternary alkali-carbonate base eutectic melt, which acted as the electrolyte. It consisted of Li<sub>2</sub>CO<sub>3</sub>, Na<sub>2</sub>CO<sub>3</sub> and K<sub>2</sub>CO<sub>3</sub> (from Sigma Aldrich, ≥99% purity) with a mole ratio of 43.5:31.5:25.0, respectively. The ratio was used to provide a eutectic melt. The alkali-carbonates were firstly dried for at least 24 h in an oven at 110 °C before being mixed in the specific molar ratio. To ensure the alkali-carbonate mixture was homogenous, it was firstly mechanically ball-milled (Fritsch Pulverisette 6, Germany) for 1 h and then thermally fused at 500 °C (heating rate of 3 °C/min) in a muffle furnace under a CO<sub>2</sub> atmosphere (flow rate of 60 mL/min) for 2 h before allowing to cool to room temperature in a CO<sub>2</sub> atmosphere.

The hard carbon samples in this work were grown with a similar experimental setup found in previously published work [17,18]. To grow the hard carbons from the carbonate mixture, a two-electrode setup was used, which was composed of a graphite rod (10 mm diameter—Alfa Aesar, Ward Hill, MA, USA) as the reference/counter electrode, and either copper foil (99.98% purity and 0.25 mm thickness), gold foil (99.99% purity, 0.25 mm thickness) or a graphite rod (6.75 mm diameter) as the working electrodes. Substrates were sealed into alumina holders using an alumina-based adhesive (Resbond 989, Cotronics, Brooklyn, NY, USA) and silver paste was used to secure electrical connections. Alumina crucibles provided a container for the eutectic melt and electrode setup. The assembly was heated to maintain a temperature of 600 °C in a CO<sub>2</sub> atmosphere for 30 min prior to deposition. Initial testing was conducted with cyclic voltammetry (CV) to check connections and current response for each experiment prior to deposition (WaveNow potentiostat using Aftermath software 1.6, Pine Research Instrumentation, Inc, Durham, NC, USA), while deposition was carried out using a GW Laboratory DC power supply (GPS-1830).

Different deposition conditions, outlined in Table 1, were used for all samples and labelled respectively. The deposited solidified carbon was manually separated from the electrolyte upon cooling and soaked in 1 M H<sub>2</sub>SO<sub>4</sub> for 24 h followed by filtration with Whatman Filter Paper (Grade 1) and rinsing with distilled water.

**Table 1.** Matrix of growth conditions for all samples.

Sample Name	Substrate	Temperature (°C)	Current Density (A/cm <sup>2</sup> )
(1) Au-600	Au	600	0.25
(2) Cu-600	Cu	600	0.25
(3) G-700	Graphite	700	0.25
(4) G-600-30	Graphite	600	0.30
(5) G-600-09	Graphite	600	0.09

Laboratory XRD patterns were collected using a PANalytical Aeris benchtop X-ray diffractometer in Bragg–Brentano geometry with a copper anode ( $\lambda = 1.5406 \text{ \AA}$ ) as the X-ray source. Various diffraction peaks pertaining to any crystalline components found within each sample were qualitatively characterized by indexing either by matching the XRD patterns against compounds in the ICSD database via the Search and Match function of PANalytical’s HighScore Plus suite (PANalytical, 5.1, Almelo, The Netherlands) [19], or by correlating the reflection *d*-spacings to compounds in the ICDD database using PDF-4+ [20]. Using GSASII, quantitative refinement of instrumental and structural parameters via the Rietveld method, which fits a model to the diffraction data using a least squares approach, was used to provide further information on the crystal structure of selected phases.

Scanning electron microscopy (SEM) analyses on the morphologies of each sample were conducted with a Hitachi S-3400 Scanning Electron Microscope, complemented with a Bruker XFlash 6130 for energy-dispersive X-ray spectroscopy (EDS) studies. Raman scattering measurements were conducted with a laser wavelength of 532 nm, calibrated using an Si standard at  $520.3 \text{ cm}^{-1}$  on a Renishaw inVia 2 Raman spectrometer. X-ray photoelectron spectroscopy (XPS) was conducted on all samples (in electrode form) using a Thermo Scientific ESCALAB250Xi at a vacuum  $< 2 \times 10^{-9} \text{ mbar}$ , with a monochromatic Al X-ray source (energy = 1486.68 eV).

Electrodes were prepared in an 8:1:1 ratio of active material, carbon black (TIMCAL Super C65), and polyvinylidene fluoride (Sigma Aldrich, Burlington, MA, USA). This was mixed and ground before dissolving in a small amount of N-methyl-2-pyrrolidone (99.5% purity, anhydrous, Sigma Aldrich) forming a slurry that was magnetically stirred overnight to ensure homogeneity. Upon sufficient mixing, the slurry was transferred onto Cu foil and pasted, using a notch bar, to a thickness of  $200 \mu\text{m}$  and dried overnight in a vacuum oven at  $100^\circ\text{C}$ . Upon drying, electrode sheets pressed to  $75 \text{ kN}$  in a hydraulic flat-plate press (MTI Corp., Richmond, CA, USA) before cutting into circular electrodes using a 12 mm hollow punch.

Electrodes were tested in CR2032 coin cells with a half-cell configuration against Na and K metal. The electrolytes used were 1 M LiPF<sub>6</sub> in EC:DMC (1:1 %vol), 0.8 M KPF<sub>6</sub> in EC:DMC (1.1 %vol), and 1 M NaPF<sub>6</sub> in EC:DMC (1:1 %vol). Investigations were carried out at a rate of 10 mA/g and with a rate capability study.

### 3. Results and Discussion

When this synthesis method was first explored for NIBs, similar current densities and temperatures were maintained, copper and graphite substrates used and the effect of post-extraction ultrasonication and washing examined [16]. In this work, the deposition parameters are explored further (see Table 1) [17,18]. Au-600, Cu-600, and G-700 were grown on different substrates with similar applied current densities (noting an increase in the temperature for G-700), while G-600-30 and G-600-09 were both grown on a graphite substrate, but had the current density varied. Note the temperature for graphite in G-600-30 was the same as Au-600 and Cu-600 but the current density was increased slightly by  $0.05 \text{ A/cm}^2$ .

XRD data and Rietveld analysis of Cu-600 displays relatively intense and sharp reflections, which were modelled with an  $\alpha\text{-Al}_2\text{O}_3$  phase [21] while the weak reflection at

$\sim 26.6^\circ 2\theta$  is associated with the 002 reflection of graphite [22] (Figure 1a,b). Au-600 and G-600-30 also display weak reflections of the  $\alpha$ -Al<sub>2</sub>O<sub>3</sub> phase (see Figure 1a). Large, broad regions between 20–30° and at  $\sim 44^\circ 2\theta$  can be attributed to the 002 and 101 reflections of an amorphous or nanocrystalline carbon phase [23]. All samples grown on graphite show a significant 002 graphite-type reflection ( $\sim 26.6^\circ 2\theta$ ) from the growth rod [16]. Additionally, G-700 shows additional weak reflections at  $\sim 21.2$ , 29.4–33.8, and  $36.9^\circ 2\theta$  while G-600-09 shows additional weak reflections at  $\sim 20.9$ , 23.9, and  $24.8^\circ 2\theta$ . The additional reflections from both these samples are distinctively different to any impurities seen in other samples from previous work [16]. The *d*-spacings of these additional peaks did not return viable results (from both ICSD and ICDD databases).

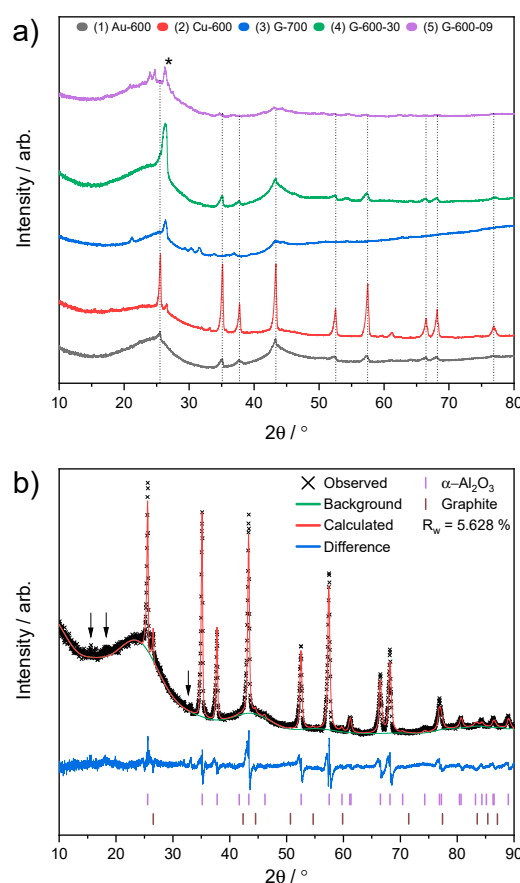


**Figure 1.** (a) Stacked plot of XRD patterns of all samples. Reflections of  $\alpha$ -Al<sub>2</sub>O<sub>3</sub> are highlighted with dotted lines, while the asterisk (\*) denotes the  $2\theta$  ( $^\circ$ ) position of the 002 reflection of graphite. (b) Rietveld analyses of Cu-600, highlighting the observed lab XRD data, the calculated background profile, calculated fit of the model to the data (with  $R_w$  %), and the difference in the fit. Peak markers for phases of  $\alpha$ -Al<sub>2</sub>O<sub>3</sub> and graphite are also shown. Black arrows indicate regions with impurities which were not indexed to any phases.

The  $\alpha$ -Al<sub>2</sub>O<sub>3</sub>, or alumina, likely originate from the alumina crucible used to hold the sample or the adhesive used during the deposition process (Resbond 989). A slight intensity mismatch between the model and majority of the  $\alpha$ -Al<sub>2</sub>O<sub>3</sub> reflections in the data in Figure 1b suggests an additional phase which can be modelled with a second  $\alpha$ -Al<sub>2</sub>O<sub>3</sub> phase with slightly different lattice parameters (see Figure S1, Supplementary Materials). This is possibly oxygen deficient or cation-substituted phases related to  $\alpha$ -Al<sub>2</sub>O<sub>3</sub>. For example, Shen et al. demonstrated that, when heated in a vacuum to above 1250 °C,  $\alpha$ -Al<sub>2</sub>O<sub>3</sub> displays oxygen deficiencies at the surface [24].

Cu-600 features large alumina particles scattered throughout the sample (Figure 2) as determined by SEM (Figure 2) and EDX (Figure S2). To a lesser extent, these particles are

also present within Au-600 and G-600-30. Figure S3 displays higher magnifications, which illustrate needle-like structures for Cu-600, G-600-30, and G-600-09. XPS data on electrodes (Figure S4) show large fluorine peaks from the PVDF binder and for Cu-600, which showed alumina in XRD data, no significant presence of Al ( $\text{Al}2\text{p}\sim74\text{ eV}$ ) [25]. This may suggest alumina fragments (such as small fragments of poorly adhered Resbond paste or crucible) as opposed to the homogeneous dissolution of alumina during heating.

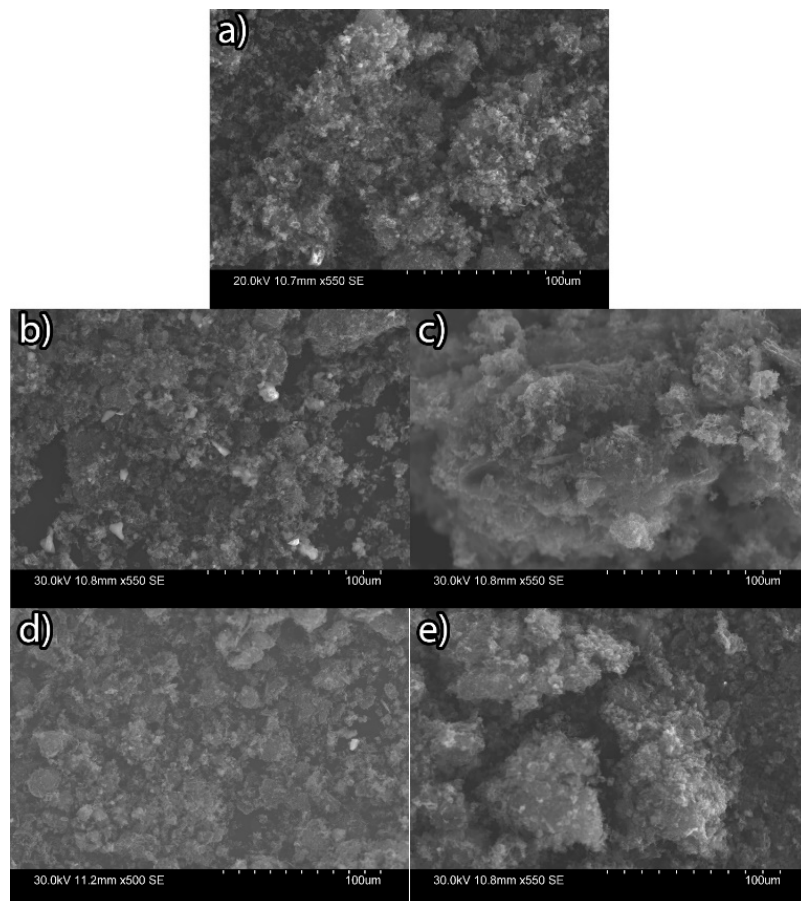


**Figure 2.** SEM images highlighting the morphologies of (a) Au-600; (b) Cu-600; (c) G-700; (d) G-600-30; and (e) G-600-09.

Raman spectroscopy data and the  $I_D/I_G$  ratios, which define the degree of disorder in the graphitic section of compounds by comparing the intensity ratio of the D ( $\sim 1350\text{ cm}^{-1}$ ) and G bands ( $\sim 1580\text{ cm}^{-1}$ ), are shown in Figure S5 and Table 2 respectively. Four regions were used to compare between the samples, with Au-600 and G-700 showing the largest variation between the regions. Cu-600, G-600-09 and G-600-30 show similar  $I_D/I_G$  ratios (Table 2) but G-600-30 displays regions of varying additional features and a shoulder peak, denoted as D', at  $\sim 1610\text{ cm}^{-1}$ , which also evidences the presence of disordering [26,27]. Interestingly, compared to Cu-600 and G-600-09, the D and G bands in G-700 are significantly sharper, which may be due to a higher degree of ordering, and thus a more graphitic material, whereas broader bands suggest the presence of a more amorphous carbon material [28]. The combination of the  $I_D/I_G$  ratios and the visual features in the Raman spectra suggest that Cu-600 and G-600-09 are the most homogeneous samples that contain amorphous carbons.

**Table 2.** Peak intensity ratios of the D and G bands of graphite ( $I_D/I_G$ ).

Sample	$I_D/I_G$			
	Region 1	Region 2	Region 3	Region 4
(1) Au-600	0.135	0.466	0.901	0.947
(2) Cu-600	0.892	0.978	0.944	0.938
(3) G-700	0.549	0.839	0.679	0.937
(4) G-600-30	0.981	0.749	0.953	0.899
(5) G-600-09	0.885	0.949	0.926	0.953

There are no significant peaks in the Raman spectra to denote the presence of  $\alpha$ -Al<sub>2</sub>O<sub>3</sub> [29] (which was observed in the XRD data) further supporting distinct alumina particles. Graphitic regions in “G” samples could arise either from the rods used for the growth, or graphite-like depositions. However, such regions in the Au sample are likely from graphite-like regions being deposited.

The long-term cycling performance and electrochemical variability analyses were undertaken and correlated to the sample’s physiochemical characterization. The focus of the work was on examining these materials against Na/Na<sup>+</sup> but similar tests were briefly performed with K/K<sup>+</sup>. Voltage and capacity curves of the 1st, 2nd, 5th, and 10th charge and discharge cycles of selected cells against Na/Na<sup>+</sup> and K/K<sup>+</sup> are shown Figures S6–S8 and briefly discussed. Figure 3 summarizes the initial electrochemical performance for all samples when cycled against Na/Na<sup>+</sup> (with K/K<sup>+</sup> shown in Figure S9). Figure 4 shows electrochemical charge–discharge curves and capacity versus cycle number as an example with these figures for all other samples shown in the Supplementary Materials.

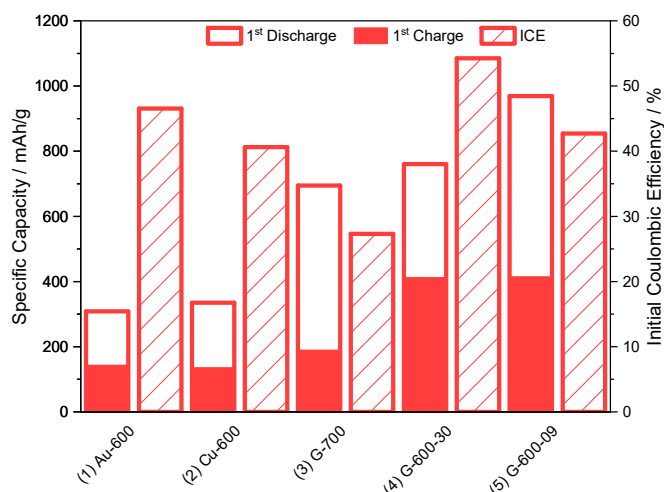


**Figure 3.** Electrochemical performance summary of selected cells, with the 1st discharge and charge capacities when cycled at 10 mA/g against Na/Na<sup>+</sup>, and the initial coulombic efficiency of the 1st charge cycle (striped bars).

Au-600 produces first discharge capacities of 309 mAh/g, reducing to ~144 mAh/g on the first charge, resulting in an initial coulombic efficiency (ICE) of 46.6%. Similarly, Cu-600 delivers first discharge capacities of 335 mAh/g, which is approx. 10% higher than Au-600, however, produces a slightly lower ICE of 40.6%. In contrast, materials grown on a graphite substrate display significantly different results where G-700 achieves initial capacities of 695 mAh/g, which decrease to 190 mAh/g to produce an ICE of only 27.3%, whilst G-600-30 achieves initial capacities of 760 mAh/g, and an ICE of 54.2%. G-600-09 displays the highest initial capacities of all samples when cycled against Na/Na<sup>+</sup>, achieving a capacity of 969 mAh/g, although producing an ICE of 42.7%. Even though these materials display low ICES, this value increases to 91.7–99.2% by the 10th cycle, with Cu-600 producing the highest, and G-700 producing the lowest.

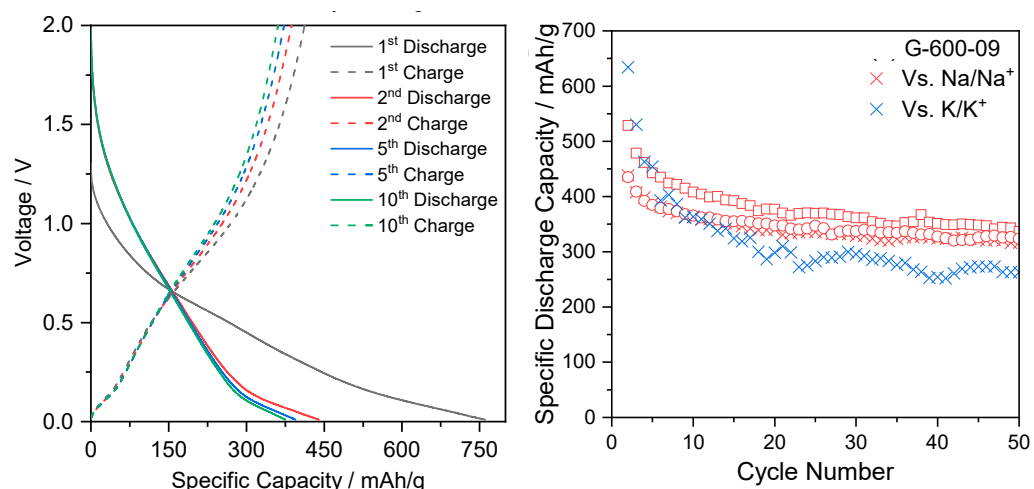


**Figure 4.** (left) G-600-09 - voltage and capacity curves of the 1st, 2nd, 5th and 10th discharge-charge cycles, at a rate of 10 mA/g against Na/Na<sup>+</sup> and (right) long-term cycling characterization, as well as variability testing against Na/Na<sup>+</sup> and K/K<sup>+</sup>.

G-600-09 displays the highest 1st discharge capacities, with G-600-30 and G-700 achieving approx. 22 and 28% less. Previously, high ICEs (88%) have been reported for amorphous carbon-based anodes for sodium-ion batteries (NIBs) [30]; however, more typical ranges of 30–70% can be found within the literature [31]. Here, samples grown on graphite show ICEs ranging from 27.3–54.2%, whilst samples deposited onto Au and Cu show ICEs of 46.5 and 40.6% respectively. With respect to samples grown on graphite, it appears that both the deposition conditions and additional phases have an adverse effect on the short-term electrochemical performance of the materials. Higher deposition temperatures of 700 °C (G-700) hinder the material's performance when cycled against Na/Na<sup>+</sup>, producing lower ICEs and capacities. G-600-30 and G-600-09, which were deposited with current densities of 0.30 and 0.09 A/cm<sup>2</sup> respectively, appear to perform differently. Overall, it appears that the trace amounts of alumina detected by XRD in G-600-30 do not significantly affect its short-term electrochemical performance. Au-600 displayed the lowest capacities of all samples. It appears that the short-term electrochemical results indicate that hard carbons grown on graphite produce significantly higher capacities than those grown on Cu or Au for Na/Na<sup>+</sup>.

Multiple reviews on the performance of hard carbon materials for use in NIBs have been explored in the literature, and while a significant proportion are derived from biomass, some are derived from plastics and rubbers [32–35]. Table 3 summarizes the electrochemical performance of hard carbons found in the literature, including the performance of a commercial hard carbon material. Although it is difficult to directly compare the electrochemical performance of electrode materials, it appears that G-600-30 and G-600-09, which were grown on graphite substrates at temperatures of 600 °C, produce high capacity electrode materials which can match, or exceed, the performance of biomass- and plastic-derived hard carbons used in NIBs.

When cycling this batch of hard carbons against K/K<sup>+</sup> (Figure S9), deposition onto an Au substrate (Au-600) appears to produce the best performing material in the short-term, with 1st discharge capacities of 2261 mAh/g, which are ~25% higher than the second-best performing material, G-600-30 (1801 mAh/g), which was grown on graphite. Although these materials produce high first discharge capacities, they suffer from low ICEs ranging from 24–30%. Interestingly, no significant differences are noted in the short-term performance between G-600-30 and G-600-09, which suggests that varying the current density of electrodeposition between 0.3 and 0.09 A/cm<sup>2</sup> has no significant effect on the electrochemical performance of these materials in K/K<sup>+</sup> systems. As with the Na/Na<sup>+</sup> examination, Cu-600 showed poor performance in K/K<sup>+</sup> systems.

**Table 3.** Comparison of the electrochemical performance of hard carbons in literature.

Precursor	Electrolyte	Capacity (mAh/g)	Cycles	Rate (mA/g)
Pomelo peel [11]	1 M NaClO <sub>4</sub> , EC/PC (1:1)	181	220	200
Sugar [36]	1 M NaClO <sub>4</sub> , EC/DEC (1:1)	324	100	20
Sugar [37]	1 M NaPF <sub>6</sub> , EC/DMC (1:1)	274	100	30
Sucrose [38]	1 M NaClO <sub>4</sub> , EC/PC (1:1)	310	20	40
Corn cob [39]	0.6 M NaPF <sub>6</sub> , EC/DMC (1:1)	275	100	60
Coconut shell [40]	1 M NaClO <sub>4</sub> , EC/DMC/FEC (88:10:2)	250	40	10
Walnut [41]	1 M NaPF <sub>6</sub> , diglyme	293	100	50
Carbotron P(J) * [42]	1 M NaClO <sub>4</sub> , EC/DEC (1:1)	230	100	25
Carbotron P(J) * [43]	1 M NaPF <sub>6</sub> , PC	250	100	25
Polyacrylonitrile [44]	1 M NaClO <sub>4</sub> , EC/DMC (1:1)	220	100	100
Kapok fibers [45]	1 M NaClO <sub>4</sub> , EC/DMC (1:1)	260	200	30
This work G-600-09	1 M LiPF <sub>6</sub> , EC:DMC (1:1)	405	50	10

\* Commercial hard carbon.

Figure 5 summarizes the average initial reversible capacities and the 5th to 50th cycle capacity retention for all samples cycled against Na/Na<sup>+</sup> where drastic distinctions in the electrochemical performance of each sample are evidenced. Similar data for K/K<sup>+</sup> can be found in Figures S10 and S11 with a brief discussion.

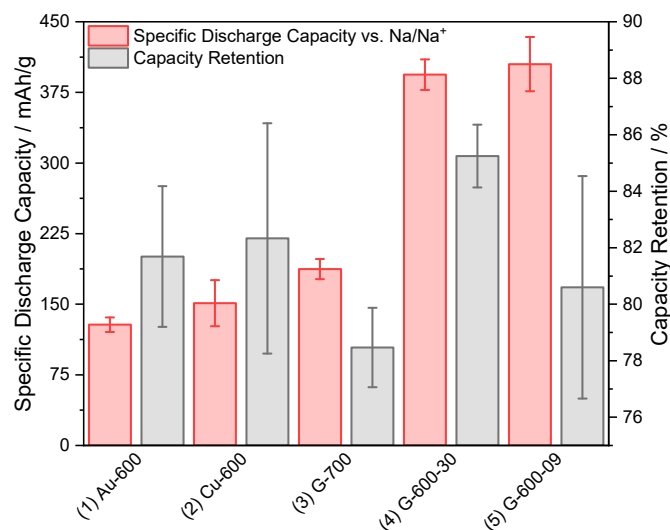


**Figure 5.** Summary of the average initial reversible capacities (red), and capacity retention (grey) between the 5th and 50th cycle, with errors, when cycled against Na/Na<sup>+</sup>.

For NIBs, microwave-treated hard carbons have shown capacities of ~300 mAh/g after 50 cycles at rates of 20 mA/g [46], while hard carbons derived from palm date waste displayed reversible capacities of up to 300 mAh/g [47]. With a cycling rate of 10 mA/g, hard carbons derived from pistachio shells have produced capacities of up to 225 mAh/g [48]. G-600-30 and G-600-09 both produced the highest initial reversible capacities of all samples when cycled against Na/Na<sup>+</sup>, with values of 394 ± 16 and 405 ± 29 mAh/g by the 5th cycle, respectively. By the 50th cycle, the capacities of G-600-30 and G-600-09 decrease to 336 ± 18 and 326 ± 10 mAh/g, respectively. While G-700, G-600-30, and G-600-09 were all deposited onto graphite, G-700 was deposited at a

higher temperature; however, this instead produced a material with lower electrochemical performance when cycled against Na/Na<sup>+</sup>.

Compared to previous Na-based work on a similar hard carbon material grown on a Cu substrate [16], Au-600 here achieves similar capacity retention, but 25–30% less initial reversible capacities. Although the Cu samples from the previous study were grown in similar conditions, it appears that the main performance-inhibiting factor in this work is the large amount of alumina present within the Cu-600 sample used, which adversely affects its electrochemical performance, producing the lowest reversible capacities of all samples. It should be noted that trace amounts of alumina were also seen in the previously reported sample [16]. This demonstrates that there is a significant need to monitor and minimize additional phase formation, especially alumina in these growths. Furthermore, in previous work [16], two samples were grown on graphite at slightly lower current densities which achieved less than 50% of the capacity observed in this work. This demonstrates that minor changes in deposition, in the case of graphite in applied current density, can have a major impact on performance. The substrate, voltage limits, current density and temperature are some of the handles that can be used to manipulate and optimize growth in order to produce the best performing samples.

Finally, cycling with Na/Na<sup>+</sup> in general shows better stability relative to K/K<sup>+</sup> in all cases. Although the samples showed exceptional first discharge capacities against K/K<sup>+</sup>, their reversible capacities were similar when compared to their performance against Na/Na<sup>+</sup>, and only Au-600 demonstrated significantly higher capacities in K/K<sup>+</sup> compared to Na/Na<sup>+</sup>.

#### 4. Conclusions

An electrochemical deposition method, which utilizes a ternary eutectic melt, has been explored to grow hard carbons on substrates of gold, copper, and graphite. The materials were structurally characterized through bulk and local environment methods and electrochemically characterized in half-cells against Na/Na<sup>+</sup> (and K/K<sup>+</sup>) at rates of 10 mA/g. XRD data indicates the presence of alumina (from the crucibles used or paste) in Au-600, Cu-600, and G-600-30 while Raman data, and I<sub>D</sub>/I<sub>G</sub> ratios indicate Cu-600 and G-600-09 produce the most homogenous materials, whilst G-700, which was deposited at a higher temperature, produces a more graphitic carbon material. The samples grown on gold and copper substrates produced the lowest capacities against Na/Na<sup>+</sup> of 145 ± 20 and 124 ± 9 mAh/g, although had consistent capacity retention of 81.7 ± 2.5 and 82.3 ± 4.1% respectively. Of the samples grown on graphite substrates, a eutectic melt temperature of 600 °C produced better performing hard carbons; however, variances in the electrochemical performance are less obvious when using current densities of 0.30 (G-600-30) or 0.09 (G-600-09) mA/cm<sup>2</sup> during the deposition. G-600-30 and G-600-09 produced similar initial capacities of 394 ± 16 and 405 ± 29 mAh/g with capacity retention of 85.2 ± 1.1 and 80.6 ± 3.9%, respectively. These are some of the highest capacities and retention observed for hard carbons reported to date. Increasing the deposition temperature to 700 °C hinders the performance of samples grown on a graphite substrate, both against K/K<sup>+</sup> and Na/Na<sup>+</sup>.

Further improvements to the electrochemical performance of these materials can be realized with a targeted evaluation of the role of additional phases. Future investigations into the reaction conditions are warranted to understand the role of parameters towards not only sample formation but also to additional phase minimization or optimization (for synergistic effects). Interestingly, modifying the growth parameters produces materials that vary in performance characteristics for electrodes in sodium- and potassium-ion batteries. This can be optimized for performance in the future.

**Supplementary Materials:** The following supporting information can be downloaded at: <https://www.mdpi.com/article/10.3390/batteries8080081/s1>, Figure S1: magnified Rietveld-refined fit of XRD data; Figure S2: EDX mapping of Cu-600; Figure S3: SEM images; Figure S4: XPS data; Figure S5: Raman spectra and optical images; Figure S6: Voltage versus capacity curves for Cu-600 and Au-600; Figure S7: Voltage versus capacity curves for the G samples; Figure S8: Summary of short term electrochemical performance; Figure S9: Electrochemical performance against K/K<sup>+</sup>; Figure S10: Long term cycling data; Figure S11: Summary of capacity retention in K/K<sup>+</sup> systems. References [16,49–51] are cited in the supplementary materials.

**Author Contributions:** J.W.—formal analysis, investigation, methodology, writing—original draft, M.A.H.—investigation, N.S. and J.A.—conceptualization, methodology, supervision, writing—review and editing. All authors have read and agreed to the published version of the manuscript.

**Funding:** This research was funded by the Australian Research Council, grant number DE210100680, DP200100959 and the research training program.

**Institutional Review Board Statement:** Not applicable.

**Informed Consent Statement:** Not applicable.

**Data Availability Statement:** Data is available from the authors.

**Acknowledgments:** J.W. and M.H. would like to thank the research training scheme. J.A. acknowledges funding from the Australian Research Council received during preparation of this work under DE210100680, and N.S. would like to acknowledge support from the Australian Research Council through the discovery program under DP200100959.

**Conflicts of Interest:** The authors declare no conflict of interest.

## References

- Choi, J.W.; Aurbach, D. Promise and reality of post-lithium-ion batteries with high energy densities. *Nat. Rev. Mater.* **2016**, *1*, 1–16. [[CrossRef](#)]
- Zimmerman, A.H. Self-discharge losses in lithium-ion cells. *IEEE Aerosp. Electron. Syst. Mag.* **2004**, *19*, 19–24. [[CrossRef](#)]
- Haregewoin, A.M.; Wotango, A.S.; Hwang, B.-J. Electrolyte additives for lithium ion battery electrodes: Progress and perspectives. *Energy Environ. Sci.* **2016**, *9*, 1955–1988. [[CrossRef](#)]
- Hesse, H.C.; Schimpe, M.; Kucevic, D.; Jossen, A. Lithium-ion battery storage for the grid—A review of stationary battery storage system design tailored for applications in modern power grids. *Energies* **2017**, *10*, 2107. [[CrossRef](#)]
- Rong, W.Q.; You, J.H.; Zheng, X.M.; Tu, G.P.; Tao, S.; Zhang, P.Y.; Wang, Y.X.; Li, J.T. Electrodeposited Binder-Free Antimony–Iron–Phosphorous Composites as Advanced Anodes for Sodium-Ion Batteries. *ChemElectroChem* **2019**, *6*, 5420–5427. [[CrossRef](#)]
- Cui, R.C.; Xu, B.; Dong, H.J.; Yang, C.C.; Jiang, Q. N/O dual-doped environment-friendly hard carbon as advanced anode for potassium-ion batteries. *Adv. Sci.* **2020**, *7*, 1902547. [[CrossRef](#)] [[PubMed](#)]
- Wang, P.; Fan, L.; Yan, L.; Shi, Z. Low-cost water caltrop shell-derived hard carbons with high initial coulombic efficiency for sodium-ion battery anodes. *J. Alloy. Compd.* **2019**, *775*, 1028–1035. [[CrossRef](#)]
- Chen, M.; Liu, Q.; Wang, S.W.; Wang, E.; Guo, X.; Chou, S.L. High-abundance and low-cost metal-based cathode materials for sodium-ion batteries: Problems, progress, and key technologies. *Adv. Energy Mater.* **2019**, *9*, 1803609. [[CrossRef](#)]
- Dou, X.; Hasa, I.; Saurel, D.; Vaalma, C.; Wu, L.; Buchholz, D.; Bresser, D.; Komaba, S.; Passerini, S. Hard carbons for sodium-ion batteries: Structure, analysis, sustainability, and electrochemistry. *Mater. Today* **2019**, *23*, 87–104. [[CrossRef](#)]
- Li, Y.; Hu, Y.S.; Titirici, M.M.; Chen, L.; Huang, X. Hard carbon microtubes made from renewable cotton as high-performance anode material for sodium-ion batteries. *Adv. Energy Mater.* **2016**, *6*, 1600659. [[CrossRef](#)]
- Hong, K.-I.; Qie, L.; Zeng, R.; Yi, Z.-q.; Zhang, W.; Wang, D.; Yin, W.; Wu, C.; Fan, Q.-J.; Zhang, W.-X. Biomass derived hard carbon used as a high performance anode material for sodium ion batteries. *J. Mater. Chem. A* **2014**, *2*, 12733–12738. [[CrossRef](#)]
- Rios, C.d.M.S.; Simone, V.; Simonin, L.; Martinet, S.; Dupont, C. Biochars from various biomass types as precursors for hard carbon anodes in sodium-ion batteries. *Biomass Bioenergy* **2018**, *117*, 32–37. [[CrossRef](#)]
- Hughes, M.A.; Allen, J.A.; Donne, S.W. Carbonate reduction and the properties and applications of carbon formed through electrochemical deposition in molten carbonates: A review. *Electrochim. Acta* **2015**, *176*, 1511–1521. [[CrossRef](#)]
- Weng, W.; Tang, L.; Xiao, W. Capture and electro-splitting of CO<sub>2</sub> in molten salts. *J. Energy Chem.* **2019**, *28*, 128–143. [[CrossRef](#)]
- Prieto, C.; Fereres, S.; Ruiz-Cabafas, F.J.; Rodriguez-Sanchez, A.; Montero, C. Carbonate molten salt solar thermal pilot facility: Plant design, commissioning and operation up to 700 C. *Renew. Energy* **2020**, *151*, 528–541. [[CrossRef](#)]
- Wu, J.; Moradmand, S.; Pang, W.K.; Allen, J.; Sharma, N. Sodium-ion battery anodes from carbon depositions. *Electrochim. Acta* **2021**, *379*, 138109. [[CrossRef](#)]

17. Hughes, M.A.; Allen, J.A.; Donne, S.W. The properties of carbons derived through the electrolytic reduction of molten carbonates under varied conditions: Part I. A study based on step potential electrochemical spectroscopy. *J. Electrochem. Soc.* **2018**, *165*, A2608. [[CrossRef](#)]
18. Hughes, M.A.; Bennett, R.D.; Allen, J.A.; Donne, S.W. Physical characteristics of capacitive carbons derived from the electrolytic reduction of alkali metal carbonate molten salts. *RSC Adv.* **2019**, *9*, 36771–36787. [[CrossRef](#)] [[PubMed](#)]
19. Degen, T.; Sadki, M.; Bron, E.; König, U.; Nénert, G. The highscore suite. *Powder Diffr.* **2014**, *29*, S13–S18. [[CrossRef](#)]
20. Kabekkodu, S.N.; Faber, J.; Fawcett, T. The powder diffraction file: Present and future. *Acta Crystallogr. Sect. B Struct. Sci.* **2002**, *58*, 333–337. [[CrossRef](#)] [[PubMed](#)]
21. Finger, L.W.; Hazen, R.M. Crystal structure and compression of ruby to 46 kbar. *J. Appl. Phys.* **1978**, *49*, 5823–5826. [[CrossRef](#)]
22. Trucano, P.; Chen, R. Structure of graphite by neutron diffraction. *Nature* **1975**, *258*, 136–137. [[CrossRef](#)]
23. Liu, X.-Y.; Huang, M.; Ma, H.-L.; Zhang, Z.-Q.; Gao, J.-M.; Zhu, Y.-L.; Han, X.-J.; Guo, X.-Y. Preparation of a carbon-based solid acid catalyst by sulfonating activated carbon in a chemical reduction process. *Molecules* **2010**, *15*, 7188–7196. [[CrossRef](#)] [[PubMed](#)]
24. Shen, P.; Fujii, H.; Matsumoto, T.; Nogi, K. Wetting of (0001)  $\alpha$ -Al<sub>2</sub>O<sub>3</sub> single crystals by molten Al. *Scr. Mater.* **2003**, *48*, 779–784. [[CrossRef](#)]
25. Kosova, N.; Devyatkina, E.; Slobodyuk, A.; Kaichev, V. Surface chemistry study of LiCoO<sub>2</sub> coated with alumina. *Solid State* **2008**, *179*, 1745–1749. [[CrossRef](#)]
26. Childres, I.; Jauregui, L.A.; Park, W.; Cao, H.; Chen, Y.P. Raman spectroscopy of graphene and related materials. *New Dev. Photon Mater. Res.* **2013**, *1*, 1–20.
27. Dresselhaus, M.S.; Kalish, R. *Ion Implantation in Diamond, Graphite and Related Materials*; Springer: Berlin/Heidelberg, Germany, 2013.
28. Bokobza, L.; Bruneel, J.-L.; Couzi, M. Raman spectra of carbon-based materials (from graphite to carbon black) and of some silicone composites. *C—J. Carbon Res.* **2015**, *1*, 77–94. [[CrossRef](#)]
29. Cava, S.; Tebcherani, S.; Souza, I.; Pianaro, S.; Paskocimas, C.; Longo, E.; Varela, J.A. Structural characterization of phase transition of Al<sub>2</sub>O<sub>3</sub> nanopowders obtained by polymeric precursor method. *Mater. Chem. Phys.* **2007**, *103*, 394–399. [[CrossRef](#)]
30. Li, Y.; Mu, L.; Hu, Y.-S.; Li, H.; Chen, L.; Huang, X. Pitch-derived amorphous carbon as high performance anode for sodium-ion batteries. *Energy Storage Mater.* **2016**, *2*, 139–145. [[CrossRef](#)]
31. He, H.; Sun, D.; Tang, Y.; Wang, H.; Shao, M. Understanding and improving the initial Coulombic efficiency of high-capacity anode materials for practical sodium ion batteries. *Energy Storage Mater.* **2019**, *23*, 233–251. [[CrossRef](#)]
32. El Moctar, I.; Ni, Q.; Bai, Y.; Wu, F.; Wu, C. Hard carbon anode materials for sodium-ion batteries. *Funct. Mater. Lett.* **2018**, *11*, 1830003. [[CrossRef](#)]
33. Zhang, H.; Huang, Y.; Ming, H.; Cao, G.; Zhang, W.; Ming, J.; Chen, R. Recent advances in nanostructured carbon for sodium-ion batteries. *J. Mater. Chem. A* **2020**, *8*, 1604–1630. [[CrossRef](#)]
34. Yu, P.; Tang, W.; Wu, F.-F.; Zhang, C.; Luo, H.-Y.; Liu, H.; Wang, Z.-G. Recent progress in plant-derived hard carbon anode materials for sodium-ion batteries: A review. *Rare Met.* **2020**, *39*, 1019–1033. [[CrossRef](#)]
35. Xiao, B.; Rojo, T.; Li, X. Hard carbon as sodium-ion battery anodes: Progress and challenges. *ChemSusChem* **2019**, *12*, 133–144. [[CrossRef](#)]
36. Prabakar, S.R.; Jeong, J.; Pyo, M. Nanoporous hard carbon microspheres as anode active material of lithium ion battery. *Electrochim. Acta* **2015**, *161*, 23–31. [[CrossRef](#)]
37. Chen, C.; Wu, M.; Liu, J.; Xu, Z.; Zaghib, K.; Wang, Y. Effects of ester-based electrolyte composition and salt concentration on the Na-storage stability of hard carbon anodes. *J. Power Sources* **2020**, *471*, 228455. [[CrossRef](#)]
38. Bommier, C.; Luo, W.; Gao, W.-Y.; Greaney, A.; Ma, S.; Ji, X. Predicting capacity of hard carbon anodes in sodium-ion batteries using porosity measurements. *Carbon* **2014**, *76*, 165–174. [[CrossRef](#)]
39. Liu, P.; Li, Y.; Hu, Y.-S.; Li, H.; Chen, L.; Huang, X. A waste biomass derived hard carbon as a high-performance anode material for sodium-ion batteries. *J. Mater. Chem. A* **2016**, *4*, 13046–13052. [[CrossRef](#)]
40. Reddy, M.A.; Helen, M.; Groß, A.; Fichtner, M.; Euchner, H. Insight into sodium insertion and the storage mechanism in hard carbon. *ACS Energy Lett.* **2018**, *3*, 2851–2857. [[CrossRef](#)]
41. Nita, C.; Zhang, B.; Dentzer, J.; Ghimbeu, C.M. Hard carbon derived from coconut shells, walnut shells, and corn silk biomass waste exhibiting high capacity for Na-ion batteries. *J. Energy Chem.* **2021**, *58*, 207–218. [[CrossRef](#)]
42. Komaba, S.; Murata, W.; Ishikawa, T.; Yabuuchi, N.; Ozeki, T.; Nakayama, T.; Ogata, A.; Gotoh, K.; Fujiwara, K. Electrochemical Na insertion and solid electrolyte interphase for hard-carbon electrodes and application to Na-Ion batteries. *Adv. Funct. Mater.* **2011**, *21*, 3859–3867. [[CrossRef](#)]
43. Dahbi, M.; Nakano, T.; Yabuuchi, N.; Ishikawa, T.; Kubota, K.; Fukunishi, M.; Shibahara, S.; Son, J.-Y.; Cui, Y.-T.; Oji, H. Sodium carboxymethyl cellulose as a potential binder for hard-carbon negative electrodes in sodium-ion batteries. *Electrochim. Commun.* **2014**, *44*, 66–69. [[CrossRef](#)]
44. Jin, J.; Shi, Z.-Q.; Wang, C.-Y. Electrochemical performance of electrospun carbon nanofibers as free-standing and binder-free anodes for sodium-ion and lithium-ion batteries. *Electrochim. Acta* **2014**, *141*, 302–310. [[CrossRef](#)]
45. Yu, Z.-E.; Lyu, Y.; Wang, Y.; Xu, S.; Cheng, H.; Mu, X.; Chu, J.; Chen, R.; Liu, Y.; Guo, B. Hard carbon micro-nano tubes derived from kapok fiber as anode materials for sodium-ion batteries and the sodium-ion storage mechanism. *Chem. Commun.* **2020**, *56*, 778–781. [[CrossRef](#)] [[PubMed](#)]

46. Li, Z.; Chen, Y.; Jian, Z.; Jiang, H.; Razink, J.J.; Stickle, W.F.; Neuefeind, J.C.; Ji, X. Defective hard carbon anode for Na-ion batteries. *Chem. Mater.* **2018**, *30*, 4536–4542. [[CrossRef](#)]
47. Izanzar, I.; Dahbi, M.; Kiso, M.; Doubaji, S.; Komaba, S.; Saadoune, I. Hard carbons issued from date palm as efficient anode materials for sodium-ion batteries. *Carbon* **2018**, *137*, 165–173. [[CrossRef](#)]
48. Kim, K.; Lim, D.G.; Han, C.W.; Osswald, S.; Ortalan, V.; Youngblood, J.P.; Pol, V.G. Tailored carbon anodes derived from biomass for sodium-ion storage. *ACS Sustain. Chem. Eng.* **2017**, *5*, 8720–8728. [[CrossRef](#)]
49. Jian, Z.; Xing, Z.; Bommier, C.; Li, Z.; Ji, X. Hard carbon microspheres: Potassium-ion anode versus sodium-ion anode. *Adv. Energy Mater.* **2016**, *6*, 1501874. [[CrossRef](#)]
50. Li, W.; Li, Z.; Zhang, C.; Liu, W.; Han, C.; Yan, B.; An, S.; Qiu, X. Hard carbon derived from rice husk as anode material for high performance potassium-ion batteries. *Solid State Ion.* **2020**, *351*, 115319. [[CrossRef](#)]
51. Wu, Z.; Wang, L.; Huang, J.; Zou, J.; Chen, S.; Cheng, H.; Jiang, C.; Gao, P.; Niu, X. Loofah-derived carbon as an anode material for potassium ion and lithium ion batteries. *Electrochim. Acta* **2019**, *306*, 446–453. [[CrossRef](#)]